



Contents lists available at ScienceDirect



Thin Solid Films

journal homepage: www.elsevier.com/locate/tsf

Vibrational properties of bulk LaAlO₃ from Fourier-transform infrared ellipsometry

Travis Willett-Gies, Eric DeLong, Stefan Zollner*

Department of Physics, New Mexico State University, MSC 3D, P.O. Box 30001, Las Cruces, NM 88003-8001, USA

ARTICLE INFO

Available online xxxx

Keywords:

Spectroscopic ellipsometry
Lanthanum aluminate
Lattice dynamics
Infrared
Dielectric function

ABSTRACT

We used Fourier-transform infrared spectroscopic ellipsometry to determine the dielectric function of twinned single-crystalline bulk lanthanum aluminate at 300 K in the region of lattice vibrations from 250 to 1000 cm⁻¹. We fit the experimental data using a classical sum of Lorentz oscillators as well as a factorized model. We were able to determine the parameters of five infrared-active optical phonons within our spectral range. Transverse phonons appear as peaks in the imaginary part of the dielectric function which are clearly visible without fitting. By transforming the data to obtain the loss function, we are able to observe the longitudinal phonons as peaks in the imaginary part. The polar nature of LaAlO₃ causes a strong splitting between the transverse optical (TO) and longitudinal optical (LO) phonon energies. We report energies, amplitudes and broadenings of five TO/LO phonon pairs and compare the two models used to describe the data.

© 2013 Elsevier B.V. All rights reserved.

1. Introduction

Lanthanum aluminate (LaAlO₃) is widely used as a substrate material in oxide epitaxy [1]. Recently, thin films of LaAlO₃ have drawn considerable attention owing to the discovery of a two-dimensional electron gas in LaAlO₃/SrTiO₃ heterostructures [2–4]. During the early development of high-k gate dielectrics, the semiconductor industry considered LaAlO₃ as a replacement for SiO₂ as a gate dielectric, mostly because of its close lattice match with Si [5–7].

LaAlO₃ is a polar perovskite with a distorted cubic crystal structure. It can be viewed as an alternating stack of positively charged LaO and negatively charged AlO₂ planes. The distortions lead to a rhombohedral structure with space group R̄3c or D_{3d}⁶ (space group 167) at room temperature [8–12]. The rhombohedral lattice constants of LaAlO₃ are found to be $a = b = 5.365 \text{ \AA}$ and $c = 13.111 \text{ \AA}$ using neutron powder diffraction [9,10]. The long-wavelength optical phonon modes expected for this crystal structure are given by the factor group [12–14]

$$\Gamma(D_{3d}^6) = 2A_{1u} + 3A_{2g} + A_{1g} + 3A_{2u} + 4E_g + 5E_u. \quad (1)$$

The relationship between the cubic $Pm\bar{3}m$ or O_h^1 perovskite phonons and the crystal field splittings due to the rhombohedral distortions are summarized in Table 1 [12–14].

Near 800 K, LaAlO₃ transforms from the rhombohedral to the cubic crystal structure [9,10,12,15]. Raman measurements of low-energy phonons with energy below 200 cm⁻¹ have revealed that there is a soft phonon [9,12] associated with this transition. The energy splitting of

the lowest-energy E_g/A_{1g} phonon pair (representing the rotation of an AlO₆ octahedron) decreases with increasing temperature. At 800 K, they merge into a zero-frequency phonon with F_{2u} symmetry [9,12].

The vibrational structure of LaAlO₃ has been studied both theoretically and experimentally. Abrashev et al. [14] calculated the long-wavelength optical phonon frequencies using a semi-empirical shell model and plotted diagrams showing the displacement patterns of the atoms involved in the vibration. They also included the splittings between transverse (TO) and longitudinal (LO) optical phonons due to the long-range polar interactions. More recently, Delugas et al. [16] presented an ab initio density-functional and self-interaction-corrected calculation of the optical phonon frequencies, in which the TO/LO splittings were ignored. None of these calculations are sufficiently accurate for comparison with experimental results for the phonon frequencies.

The factor group analysis in Eq. (1) describes the symmetry of the optical phonons and how they can be observed experimentally. The results are summarized in Table 1: One A_{1g} mode and four E_g modes are Raman active. Three A_{2u} and five E_u modes are infrared active and can be observed with Fourier-transform infrared (FTIR) ellipsometry. Finally, two A_{1u} modes and three A_{2g} modes are silent and not accessible experimentally using first-order Raman or infrared measurements.

While most Raman spectroscopy studies have focused on the temperature dependence of the A_{1g} and E_g soft modes and their implications about the phase transition from the rhombohedral to the cubic crystal structure [9,12,14], the higher-energy Raman modes have also been investigated [12,14]. Four Raman modes have clearly been identified, while the assignment of the fifth mode is controversial. See Table 1 for a summary of experimental results.

The IR-active modes have been investigated by infrared reflectance or transmittance measurements, usually followed by fitting of the dielectric function as a sum of Lorentz oscillators [13,17–19]. Three pairs

* Corresponding author.

E-mail address: zollner@nmsu.edu (S. Zollner).

Table 1

Summary of transverse optical phonon modes for LaAlO₃ at 300 K. All energies are listed in units of cm⁻¹.

R3c symmetry	Pm $\bar{3}$ m symmetry	Activity	Pattern	Energy (exp)
E _g	F _{2u} (R)	Raman	AlO ₆	33 ^a
A _{1g}	F _{2u} (R)	Raman	AlO ₆	123 ^b
E _g	F _{1u} (R)	Raman	La	152 ^b
E _g	F _{1u} (R)?	Raman	O	470 ^b (?)
E _g	E _u (R)?	Raman	O	487 ^b
A _{2u}	F _{1u} (T)	IR	AlO-La	188(1) ^c
A _{2u}	F _{1u} (T)	IR	O bend	427.0(1) ^c
A _{2u}	F _{1u} (T)	IR	O stretch	650.79(5) ^c
E _u	F _{1u} (T)	IR	AlO-La	188(1) ^c
E _u	F _{2u} (T)	IR	O	weak
E _u	F _{1u} (T)	IR	O bend	427(1) ^c
E _u	F _{2g} (R)	IR	Al	495.72(1) ^c
E _u	F _{1u} (T)	IR	O stretch	708.2(9) ^c
A _{1u}	F _{2u} (T)	silent		NA
A _{1u}	F _{2g} (R)	silent	Al	NA
A _{2g}	F _{1u} (R)	silent	La	NA
A _{2g}	F _{1u} (R)	silent	O	NA
A _{2g}	A _{2u} (R)	silent		NA

^a Ref. [12].

^b Ref. [14].

^c This work using Eq. (4).

of A_{2u}/E_u modes, arising from the crystal field splitting of the three cubic F_{1u}(T) modes, lead to strong features in the spectra [14]. One weak zone-folded E_u mode is also seen clearly, while the second E_u mode (derived from F_{2u}, which is silent in the cubic parent structure) has been considered too weak to be observable [14]. There is considerable disagreement in the literature about the exact phonon energies, amplitudes, and broadenings used to fit experimental spectra.

In this work, we determined the energies, broadenings, and amplitudes of the infrared-active optical phonons with very high accuracy using Fourier-transform infrared ellipsometry. We also describe the symmetries of all phonons and their relationships, such as rhombohedral splittings and the relationship to their cubic phonon counterparts.

2. Experiment and models

Two single-sided polished, 2-inch LaAlO₃ wafers with 0.5 mm thickness and (100) surface orientation were obtained commercially [20]. To reduce the reflections from the backside, one wafer was roughened further using a bead blaster. Our substrates are twinned and the surface orientation refers to the pseudo-cubic structure. Additional information about the samples and their properties are given in our earlier work [21], where we also report the dielectric function of LaAlO₃ from 0.8 to 6.6 eV between 77 and 700 K. Most importantly for the present work, our earlier research found $\epsilon_{\infty} = 4.12 \pm 0.01$ at 300 K.

Infrared ellipsometry measurements were performed on a J.A. Woollam FTIR-VASE variable angle of incidence ellipsometer at the Center for Integrated Nanotechnologies user facility. This instrument is based on a fixed analyzer (at 0° and 180°), a fixed polarizer (at ± 45°), and a rotating compensator. To increase accuracy, two fixed positions for the analyzer and polarizer were chosen (four-zone measurements), as this cancels experimental errors to first order in the analyzer and polarizer position. We measured at four angles of incidence: 60°, 65°, 70°, and 75°. Nominally, the instrument reports data between 250 and 8000 cm⁻¹ but we restrict our analysis to the region of the lattice vibrations between 250 and 1000 cm⁻¹. We did not observe features in the spectra above 1000 cm⁻¹ other than normal dispersion. In the spectral range around 6000 cm⁻¹, our FTIR ellipsometry results are consistent with our earlier near-IR work [21].

For various reasons, FTIR ellipsometry measurements on a bulk LaAlO₃ wafer are quite challenging. On one hand, the reflectance of LaAlO₃ is quite low (about 11% at normal incidence in the mid-IR), much lower than for a bulk semiconductor or for a thin film on Si. In

the region of the lattice vibrations, the reflectance becomes very small [18,22] near 300, 620, and 800 cm⁻¹. On the other hand, the phonon broadenings in LaAlO₃ are very low (near 4 cm⁻¹ or less). We therefore select a resolution of 2 cm⁻¹ for the FTIR spectrometer. These conditions create noise below 350 and near 800 cm⁻¹. We are thus forced to select a data acquisition time of eight hours to improve the signal to noise ratio, using 20 FTIR scans per spectrum and 15 spectra for each revolution of the rotating compensator.

Spectroscopic ellipsometry measures the ellipsometric angles ψ and Δ as a function of photon energy. These ellipsometric angles and the Fresnel reflectance ratio $\rho = e^{i\Delta} \tan \psi$ are related to the pseudo-refractive index \hat{n} and the pseudo-dielectric function $\hat{\epsilon} = \hat{n}^2$ of the sample through [23,24]

$$\rho = \frac{(\hat{n} \cos \phi_0 - \cos \phi_1)(\cos \phi_0 + \hat{n} \cos \phi_1)}{(\hat{n} \cos \phi_0 + \cos \phi_1)(\cos \phi_0 - \hat{n} \cos \phi_1)}, \quad (2)$$

where ϕ_0 is the angle of incidence and ϕ_1 the angle of refraction. For an ideal sample without surface overayers, \hat{n} and $\hat{\epsilon}$ are equal to the refractive index n and the dielectric function $\epsilon = n^2$. Δ equals zero or π for an ideal transparent substrate (for an insulator outside of the region of lattice vibrations), because all quantities in Eq. (2) are real. For our LaAlO₃ substrates, the surface overayers are very thin (see Table I in Ref. [21]). The surface roughness is between 15 and 20 Å for our samples.

Normally, spectroscopic ellipsometry requires extensive data analysis to determine the optical constants (the complex dielectric function $\epsilon = n^2$) from the ellipsometric angles. This is not the case for our analysis. We can simply convert the measured ellipsometric angles into the dielectric function using Eq. (2), because the effect of surface roughness is negligible. The transverse optical (TO) phonons appear as peaks in the dielectric function [25,26]. Longitudinal optical (LO) vibrations are possible at energies where $\epsilon(\omega) = 0$. LO phonons therefore appear as peaks in the loss function $\text{Im}(-1/\epsilon)$.

To determine accurate phonon energies, amplitudes, and broadenings, we write the dielectric function ϵ as a function of photon energy ω as a sum of uncoupled damped harmonic oscillators [25–27]

$$\epsilon(\omega) = \epsilon_{\infty} + \sum_i \frac{A_i \omega_i^2}{\omega_i^2 - \omega^2 - i\gamma_i \omega}. \quad (3)$$

The first term $\epsilon_{\infty} = 4.12 \pm 0.01$ (see Ref. [21]) describes the contributions of electronic transitions to the dielectric function. In principle, we expect eight terms in the sum, one for each infrared active phonon. In practice, some of these phonons may be very weak, while others may be degenerate. Normally, we use five oscillators as described below.

The Lorentz model (3) is derived for charges oscillating in an electric field. This model is classical and it assumes that the frictional force acting on the charge is proportional to their velocity [25]. This results in harmonic damping and a constant broadening term. (The LO broadening parameter is generally different from the TO broadening, most often larger, but not independent.)

The anharmonic coupling of phonons causes the decay of optical phonons into acoustic or other optical phonons with lower energy. Usually, the decay products are zone-edge phonons with a high density of states. If the splitting between the TO and LO phonons is large, then they will have different decay paths and their damping constants γ_{TO} and γ_{LO} may differ. Therefore, the uncoupled Lorentz oscillator model (3) often gives a good description of experimental data, which can be improved by assigning different damping parameters to LO and TO phonons yielding [26–29]

$$\epsilon(\omega) = \epsilon_{\infty} \prod_i \frac{\omega_{i,\text{LO}}^2 - \omega^2 - i\gamma_{i,\text{LO}}\omega}{\omega_{i,\text{TO}}^2 - \omega^2 - i\gamma_{i,\text{TO}}\omega} \quad (4)$$

as the functional form for the infrared dielectric function of insulators. If we set $\gamma_{i,\text{TO}} = \gamma_{i,\text{LO}} = \gamma_i$, then both descriptions (3) and (4) become

equivalent (at least for a single oscillator or for clearly separated narrow absorption lines) [22,26,28].

3. Experimental results

The ellipsometric angles ψ and Δ from 250 to 1000 cm⁻¹ for LaAlO₃ at 300 K are shown in Fig. 1. The data were taken at four angles of incidence (60°, 65°, 70°, and 75°). The shape of the ψ spectra can be understood using arguments presented by Humlíček [22] for α -quartz: The first reststrahlen band with $\psi = 45^\circ$ extends from the lowest TO phonon energy at 188 cm⁻¹ (below our spectral range) to the corresponding LO phonon near 280 cm⁻¹. ψ then drops to a minimum located at an energy that increases with the angle of incidence. The second reststrahlen band ($\psi = 45^\circ$) extends from 427 cm⁻¹ to 596 cm⁻¹. It is interrupted by a small dip at 496 cm⁻¹ due to the third phonon. The energy of the second minimum also increases with the angle of incidence. The third reststrahlen band has an irregular shape with contributions from two TO phonons located between 650 and 710 cm⁻¹. After the third reststrahlen band, ψ drops again. For an angle of incidence of 60°, ψ reaches zero at 1200 cm⁻¹. ψ converges to a steady state determined by ϵ_∞ near 2000 cm⁻¹. ψ never rises above 45°, which would be a sign of optical anisotropy [22]. ψ increases and decreases smoothly at the reststrahlen bands (another potential sign of crystal anisotropy found in SiC) [30].

The mid-IR Brewster angle given by $\tan\phi_B = \sqrt{\epsilon_\infty}$ is 63.8°. Therefore, in the mid-IR, $\Delta = \pi$ for our measurements at an angle of incidence of $\phi = 60^\circ$, while $\Delta = 0$ for $\phi = 65^\circ$ or larger. ϵ drops below 3 at 1200 cm⁻¹ and thus $\Delta = 0$ between 800 and 1000 cm⁻¹ for all our incidence angles. Just below the main phonon peak at 427 cm⁻¹, ϵ_1 is very large and therefore the Brewster angle is above 75°. Therefore, $\Delta = \pi$ in this range for our incidence angles (60° to 75°). ϵ_1 drops below the main phonon resonance (427 cm⁻¹) and therefore Δ drops to 0 as the Brewster angle crosses the angle of incidence. The weaker TO phonons between 495 and 710 cm⁻¹ cause more gradual changes in Δ . Below 300 cm⁻¹, Δ rises again due to the influence of the TO phonon at 188 cm⁻¹ (below our spectral range).

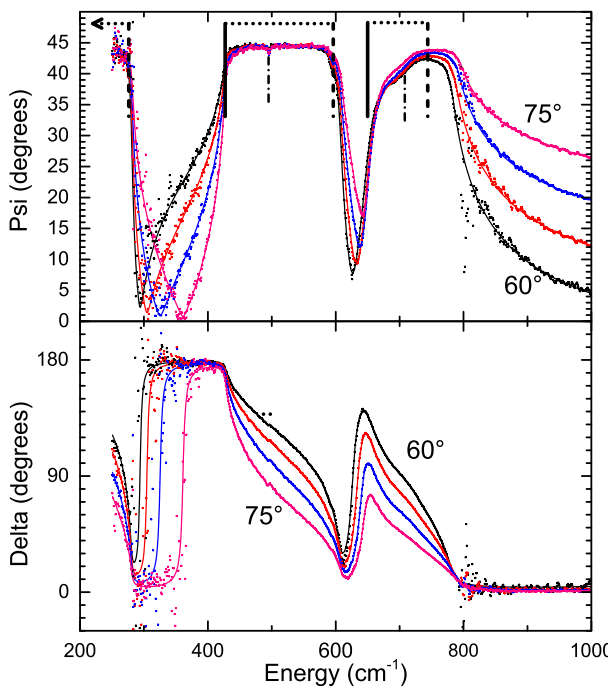


Fig. 1. (Color online) Ellipsometric angles ψ (top) and Δ (bottom) for LaAlO₃ at 300 K at four angles of incidence from 60° to 75°. Symbols: experimental data. Lines: fit with Eq. (4) and parameters in Table 3. Solid and dashed vertical lines indicate the location of transverse and longitudinal optical phonons, respectively.

An excellent description of the ellipsometric angles can be achieved using a fit with the Lorentz model in Eq. (3) and the parameters in Table 2. The average mean square deviation between our experimental data and the Lorentz model is only 40% larger than the experimental errors. The low-frequency dielectric constant is given by [25]

$$\epsilon_0 = \epsilon_\infty + \sum_i A_i = 23.81 \pm 0.06 \quad (5)$$

using the parameters in Table 2. The dominant contribution arises from the strong TO phonons at 188 and 427 cm⁻¹. This infrared optical measurement is in excellent agreement with electrical measurements [31] at 145 GHz and with density functional calculations [16].

An even better description of our experimental data (where the mean square deviation is slightly smaller than the experimental errors) is achieved with Lowndes' model in Eq. (4) and the parameters in Table 3. At the scale in Fig. 1, it is not possible to pinpoint the improvements in the fit with the Lowndes model compared to the Lorentz oscillator model.

Therefore, we compare the dielectric functions and loss functions for both models in Figs. 2, 3, 4 and 5. As a reminder, TO phonons appear as peaks in ϵ_2 and LO phonons appear as peaks in $\text{Im}(-1/\epsilon)$. The Lorentz model has the following issues describing the experimental data, which are clearly improved by the Lowndes model: (1) The minimum and maximum of ϵ_1 between 600 and 700 cm⁻¹ are too shallow. (2) The asymmetry of the peak in ϵ_2 at 650 cm⁻¹ is not described well. See especially near 600 cm⁻¹. (3) The minima and maxima in $\text{Re}(-1/\epsilon)$ and the peaks in $\text{Im}(-1/\epsilon)$ are too shallow.

The static dielectric constant can also be calculated from Eq. (4) by setting $\omega = 0$, leading to the common Lyddane-Sachs-Teller (LST) relation for multiphonon systems

$$\epsilon_0 = \epsilon_\infty \prod_i \frac{\omega_{i,\text{LO}}^2}{\omega_{i,\text{TO}}^2} = 22.3 \pm 0.3 \quad (6)$$

with parameters and errors taken from Table 3. The largest sources of error are uncertainties in the high-frequency dielectric constant ϵ_∞ and the lowest TO phonon energy (which is a fit parameter, but below our spectral range). Since the Lowndes model (4) gives a better description than the Lorentz model (3), we believe that the LST relation (6) gives a more accurate value of ϵ_0 than Eq. (5), despite the larger error bar.

Finally, we note that our data show no evidence of a weak E_u phonon peak expected at 300 cm⁻¹. Our data is very noisy at such long-wavelengths. We do not find any “ghost” peaks at other energies.

4. Discussion

Our infrared ellipsometry data yield very accurate phonon parameters for the Lorentz model (see Table 2) and the Lowndes model (see Table 3). We find that the Lowndes model gives a superior description of the experimental results, especially at peaks in the loss function related to LO phonons. This result is not surprising, since the main feature of

Table 2

Transverse optical phonon mode parameters (amplitude A , TO phonon energy ω , and TO phonon broadening γ) for LaAlO₃ at 300 K using a Lorentz oscillator fit as in Eq. (3). 90% confidence limits for experimental results are given in parentheses. The additional parameter $\epsilon_\infty = 4.12 \pm 0.01$ was fixed based on our earlier work [21].

Mode	A_i (Exp) (1)	ω_i (Exp) cm ⁻¹	γ_i (Exp) cm ⁻¹
AlO-La	15.24(5)	182(f)	4(f)
O bend	4.121(7)	426.94(6)	3.7(1)
Al	0.008(1)	495.8(3)	3.8(7)
O stretch	0.285(1)	652.9(1)	21.3(1)
O stretch	0.031(1)	688.6(3)	31.4(5)

Table 3

Transverse (TO) and longitudinal (LO) optical phonon energies and broadenings for LaAlO₃ at 300 K derived from a Lowndes oscillator fit as in Eq. (4), in units of cm⁻¹. 90% confidence limits are given in parentheses. The additional parameter $\epsilon_{\infty} = 4.12 \pm 0.01$ was fixed based on our earlier work [21].

mode	$\omega_{i,\text{TO}}$	$\gamma_{i,\text{TO}}$	$\omega_{i,\text{LO}}$	$\gamma_{i,\text{LO}}$
AlO-La	188(1)	0.4(1)	276.4(2)	3.7(7)
O bend	427.0(1)	5.0(1)	596.1(7)	7.2(1)
Al	495.72(1)	3.8(7)	495.5(3)	3.8(7)
O stretch	650.79(5)	22.5(7)	744.1(9)	12.1(1)
O stretch	708.2(9)	55.3(9)	702.2(9)	66(1)

the Lowndes model is the assignment of independent broadening parameters to the LO phonons, while the Lorentz model describes both TO and LO phonons with one broadening parameter.

For isolated strong phonon modes, both models yield nearly identical TO phonon energies (compare Tables 2 and 3). However, if two TO phonon peaks overlap, then the two models find significantly different TO phonon energies. This is true especially for the weak E_u oxygen stretch mode at 709 cm⁻¹. In general, the TO phonon energy from our model is lower than the LO phonon energy (as expected), but there is an exception for the very weak phonon located at 497 cm⁻¹, where the LO-TO separation is small and negative. In our analysis, the negative Coulomb splitting for the Al mode is only 0.2 cm⁻¹, much smaller than the resolution of our spectra (2 cm⁻¹). It is possible that a good fit to our raw data could also be found with a positive Coulomb splitting for the Al mode at 496 cm⁻¹. The weak phonon mode near 705 cm⁻¹ is also inverted, but the splitting is ten times smaller than its phonon broadening. There has been some discussion in the literature about the sign of the TO/LO phonon splitting in quartz and complex metal oxides, which we did not find convincing [33–35].

Based on an argument presented by Lowndes [29] and a generalized condition for multi-phonon systems in Ref. [36], we expect that the LO broadening should be larger than the TO broadening for a material like GaAs with a single TO-LO phonon pair. This result is confirmed for most phonon modes, except for the anomalously small LO phonon broadening of the LO phonon with the largest energy. The broadenings

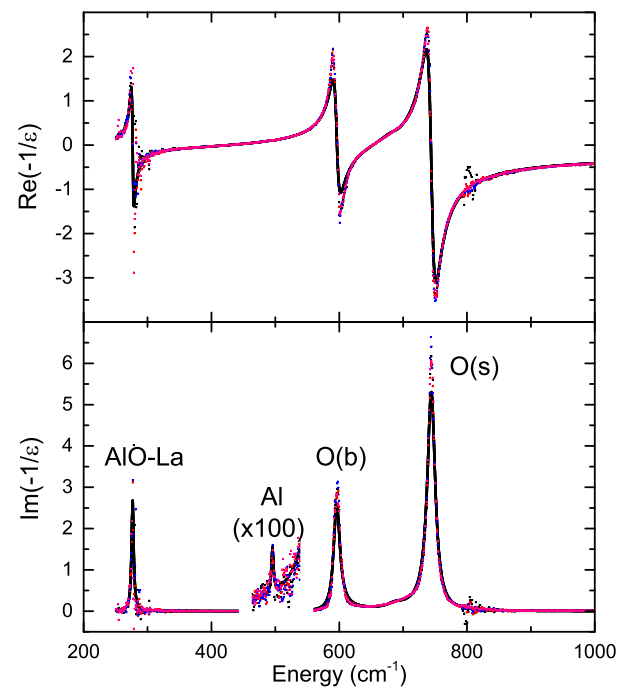


Fig. 3. (Color online) Loss function – $1/\epsilon$ for LaAlO₃ at 300 K calculated from the data in Fig. 1 using Eq. (2). Symbols: experimental data. Lines: fit with Eq. (3). Peaks corresponding to longitudinal optical phonons are found at 277, 596, 703, and 744 cm⁻¹.

of the two highest-energy phonons can also be found by visual inspection of ϵ_2 and $\text{Im}(-1/\epsilon)$ in Figs. 4 and 5. The ϵ_2 spectrum shows a sharper TO phonon at a lower energy (near 650 cm⁻¹) and a much broader TO phonon at a higher energy. Similarly, the loss function $\text{Im}(-1/\epsilon)$ shows a broad TO phonon at about 700 cm⁻¹ accompanied by a sharper LO phonon at a higher energy. Therefore, the broadenings of the TO and LO phonons at the two highest energies are a direct experimental observation, not a numerical artifact.

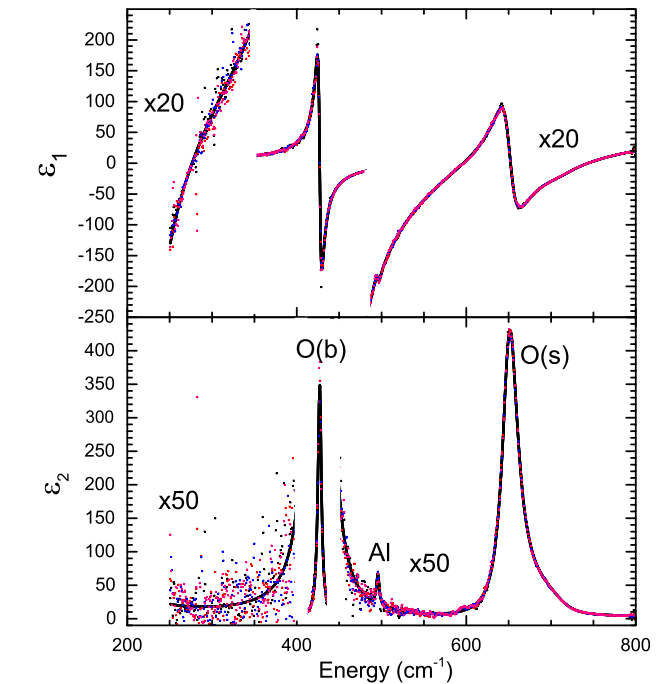
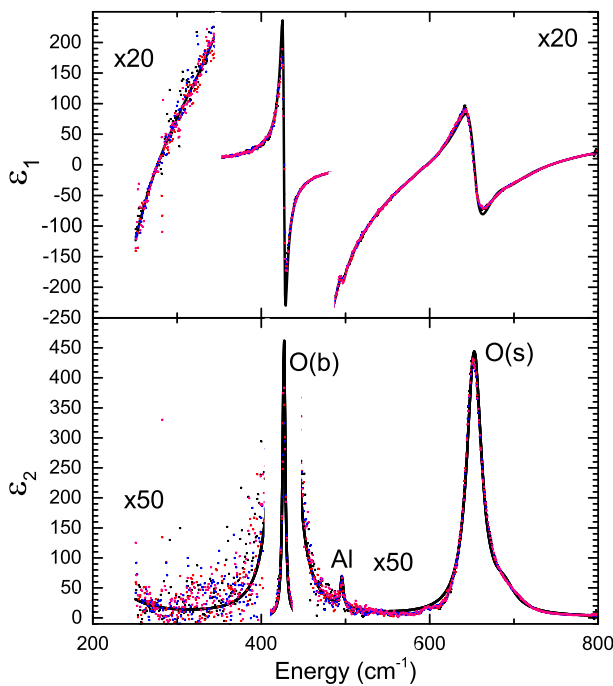


Fig. 4. (Color online) Pseudodielectric function for LaAlO₃ at 300 K calculated from the data in Fig. 1 using Eq. (2). Symbols: experimental data. Lines: fit with Eq. (4).

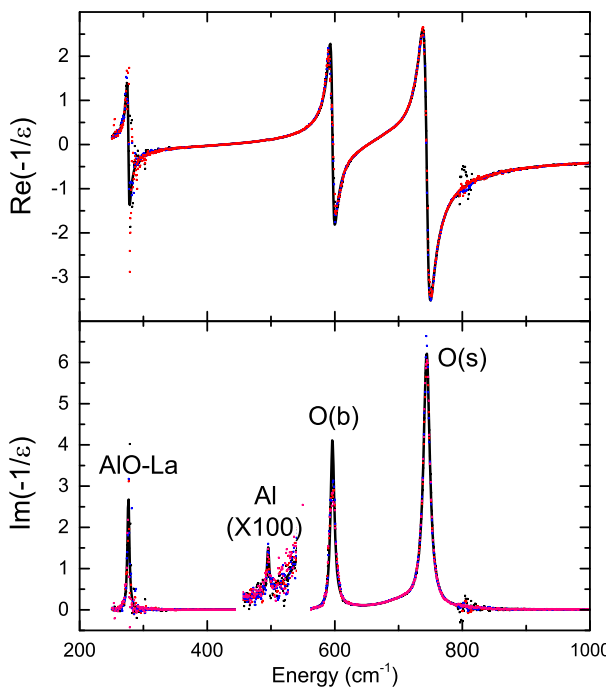


Fig. 5. (Color online) Loss function — $1/\epsilon$ for LaAlO_3 at 300 K calculated from the data in Fig. 1 using Eq. (2). Symbols: experimental data. Lines: fit with Eq. (4).

Table 4

Comparison of our experimental FTIR ellipsometry results (last column) with theory and previous FTIR reflectance measurements. TO and LO phonon energies are in units of cm^{-1} . 90% confidence limits are given in parentheses.

Mode	Theory	Theory	Reflectance	Ellipsometry
	[14]	[16]	[17]	(this work)
	TO/LO	TO	TO	TO/LO
A_{2u}	213/263	168	182	188(1)/276.4(2)
E_u	220/263	179		
E_u	270/270	297		
A_{2u}	366/496	409	429	427.0(1)/596.1(7)
E_u	371/475	411		
E_u	481/505	478	501	495.72(1)/495.5(3)
A_{2u}	706/712	627	657	650.79(5)/744.1(9)
E_u	707/712	637	695	708.2(9)/702.2(9)

A comparison of our FTIR ellipsometry results with previous FTIR reflectance measurements and theoretical results is given in Table 4.

5. Conclusions

We have characterized the parameters of the five IR-active optical phonons of LaAlO_3 . We were able to find the energies, amplitudes, and broadenings not only of the reasonably well-documented TO phonons, but also of the LO phonons which have not previously been determined experimentally. Combining our Lorentz amplitudes with the ϵ_∞ previously determined by Nelson et al. [21], we have found an experimental dielectric constant of about 22–24. This agrees well with published values for LaAlO_3 which range from 23 to 25 [32]. By characterizing

both the TO and LO phonons, we have a more complete picture of the lattice dynamics of our material. This is vital when considering the possible applications of LaAlO_3 in microelectronics.

Acknowledgments

This work was supported by the National Science Foundation (DMR-1104934). This work was performed, in part, at the Center for Integrated Nanotechnologies, an Office of Science User Facility operated for the U.S. Department of Energy (DOE) Office of Science by Los Alamos National Laboratory (Contract DE-AC52-06NA25396) and Sandia National Laboratories (Contract DE-AC04-94AL85000). We are grateful to Dr. Igal Brener for training on the operation of the FTIR ellipsometer.

References

- B.J. Gibbons, S. Trolier-McKinstry, IEEE Trans. Appl. Supercond. 7 (1997) 2177.
- A. Ohlomo, H.Y. Hwang, Nature (London) 427 (2004) 423.
- J. Mannhart, D.G. Schlom, Science 327 (2010) 1607.
- J.K. Lee, A.A. Demkov, Phys. Rev. B 78 (2008) 193104.
- S.-G. Lim, S. Kriventsov, T.N. Jackson, J.H. Haeni, D.G. Schlom, A.M. Balbashov, R. Uecker, P. Reiche, J.L. Freeouf, G. Lucovsky, J. Appl. Phys. 91 (2002) 4500.
- X.-B. Lu, Z.-G. Liu, Y.-P. Wang, Y. Yang, X.-P. Wang, H.-W. Zhou, B.-Y. Nguyen, J. Appl. Phys. 94 (2003) 1229.
- A.A. Knizhnik, I.M. Iskandarova, A.A. Bagatur'yants, B.V. Potapkin, L.R.C. Fonseca, A. Korkin, Phys. Rev. B 72 (2005) 235329.
- C. de Rango, G. Tsoucaris, C. Zelwer, Acta Crystallogr. 20 (1966) 590.
- S.A. Hayward, F.D. Morrison, S.A.T. Redfern, E.K.H. Salje, J.F. Scott, K.S. Knight, S. Tarantino, A.M. Glazer, V. Shuvava, P. Daniel, M. Zhang, M.A. Carpenter, Phys. Rev. B 72 (2005) 054110.
- C.J. Howard, B.J. Kennedy, B.C. Chakoumakos, J. Phys. Condens. Matter 12 (2000) 349.
- X. Luo, B. Wang, J. Appl. Phys. 104 (2008) 073518.
- J.F. Scott, Phys. Rev. 183 (1969) 823 (Phys. Rev. B 1, 942 (1970) (E)).
- M.C. Saine, E. Husson, H. Brusset, Spectrochim. Acta A 37 (1981) 985.
- M.V. Abrashev, A.P. Litvinchuk, M.N. Iliev, R.L. Meng, V.N. Popov, V.G. Ivanov, R.A. Chakalov, C. Thomsen, Phys. Rev. B 59 (1999) 4146.
- K.A. Müller, W. Berlinguer, F. Waldner, Phys. Rev. Lett. 21 (1968) 814.
- P. Delugas, V. Fiorentini, A. Filipetti, Phys. Rev. B 71 (2005) 134302 (This reference lists incorrect symmetries for the silent modes in Table II, which are corrected in our Table 1).
- P. Calvani, M. Capizzi, F. Donato, P. Dore, S. Lupi, P. Maselli, C.P. Varsamis, Physica C 181 (1991) 289.
- Z.M. Zhang, B.I. Choi, M.I. Flik, A.C. Anderson, J. Opt. Soc. Am. B 11 (1994) 2252.
- T. Shimada, K. Kakimoto, H. Ohsato, J. Eur. Ceram. Soc. 25 (2005) 2901 (This reference lists an incorrect space group and therefore also an incorrect factor group. It also misinterprets the experimental implications of the factor group regarding the number of observable phonon modes).
- MTI Corporation, Richmond, CA, USA.
- C.M. Nelson, M. Spies, L.S. Abdallah, S. Zollner, Y. Xu, H. Luo, J. Vac. Sci. Technol. A 30 (2012) 061404.
- J. Humlíček, Philos. Mag. B 70 (1994) 699.
- H.G. Tompkins, W.A. McGahan, Spectroscopic Ellipsometry and Reflectometry, Wiley, New York, 1999.
- H. Fujiwara, Spectroscopic Ellipsometry, Wiley, Chichester, UK, 2007.
- A.S. Barker, Phys. Rev. 136 (1964) A1290.
- F. Gervais, B. Piriou, J. Phys. C Solid State 7 (1974) 2374.
- We adopt the notation $\epsilon = \epsilon_1 + i\epsilon_2$, which results from time-period functions of the form $\exp(-i\omega t)$.
- D.W. Berreman, F.C. Unterwald, Phys. Rev. 174 (1968) 791.
- R.P. Lowndes, Phys. Rev. B 1 (1970) 2754.
- T.E. Tiwald, J.A. Woollam, S. Zollner, J. Christensen, R.B. Gregory, T. Wetteroth, S.R. Wilson, A.R. Powell, Phys. Rev. B 60 (1999) 11464.
- L.F. Edge, D.G. Schlom, P. Sivasubramani, R.M. Wallace, B. Holländer, J. Schubert, Appl. Phys. Lett. 88 (2006) 112907.
- G. Murtaza, I. Ahmad, J. Appl. Phys. 111 (2012) 123116.
- A. Chopelas, A.M. Hofmeister, Phys. Chem. Miner. 18 (1991) 279.
- J.F. Scott, S.P.S. Porto, Phys. Rev. 161 (1967) 903.
- C.J. Zollner, T. Willett-Gies, Thin Solid Films (2013) (this volume).
- M. Schubert, T.E. Tiwald, C.M. Herzinger, Phys. Rev. B 61 (2000) 8187.